2016

Fracture and toughening of soft elastic composite

Xiangchao Feng
Iowa State University

Fracture and toughening of soft elastic composite

by

Xiangchao Feng

A thesis submitted to the graduate faculty

in partial fulfillment of the requirements for the degree of

MASTER OF SCIENCE

Major: Aerospace Engineering

Program of Study Committee:
Wei Hong, Major Professor
Ashraf Bastawros
Liming Xiong

Iowa State University

Ames, Iowa

2016

TABLE OF CONTENTS

ACKNOWLEDGMENTS

I would like to thank my committee chair, Dr. Wei Hong for his patient guidance and support throughout the course of this research.

In addition, I would also like to thank my friends, colleagues, the department faculty and staff for making my time at Iowa State University a wonderful experience.

ABSTRACT

Characterized by their low modulus and high stretchability, soft composites have recently attracted great interest from researchers in related areas. The main objective of the present study is on the fracture property and toughening mechanism of soft composites. Two types of soft composites will be studied: soft elastic foam and the double-network (DN) composite. A theoretical/numerical study is carried out over soft elastic foams. By using the analogy between the cellular structure of foams and the network of rubbery polymers, a scaling law for the fracture energy is proposed for soft elastic foams. A phase-field model for the fracture processes in soft elastic structures is further developed to study the crack propagation in an elastic foam, and results have all achieved good agreement with the scaling law. Simulations have shown that an effective fracture energy one order of magnitude higher than the base material can be reached by using the soft foam structure. To further enhance the fracture and mechanical toughness, the second part of the thesis presents a combined experimental and theoretical study of the DN soft composite, which consists of stacked layers of fabric mesh and 3M VHB tapes. The composite exhibits a damage evolution process very similar to that in the well-known DN hydrogels. The testing results show that the strength and toughness of the DN composite is highly dependent on the composition, and in certain range, the DN composite exhibits much higher mechanical strength and toughness compared with the base materials. A 1D shear-lag model is developed to illustrate the damage-distribution toughening mechanism of the double network composite. The prediction of the model agrees well with the measured properties of the composite in various compositions. The DN composite may also be regarded as a macroscopic model of the DN gel for understanding its structure-property relation.

CHAPTER I

INTRODUCTION

1.1 Single network soft elastic foam

Solid foam, a state of material characterized by the highly porous cellular structure, is commonly found in nature and in everyday life. In industrial applications, solid foams are well known for their superior energy-absorbing capability under compression [2-4]. Their fracture properties have also attracted great interests [4-9]. Scaling laws between fracture properties and porosity have been proposed and widely accepted [4,5]. However, most existing theories are based on linear elastic fracture mechanics and the cell walls of the foams are assumed to be linear elastic prior to rupture. While such theories and predictions can be applied to foams of relatively stiff materials (e.g. ceramics and metals), their applicability becomes questionable to those consisting of soft and highly stretchable materials, such as elastomers. For example, an early experimental study on polyurethane foams found the fracture energy to be less dependent on the density, and even exhibiting a slight decrease when density increases [10], while the scaling laws of rigid foams all demonstrate linear or power-law dependence of the fracture energy over density [4,5].

The major difference between stiff brittle foam and soft elastic foam lies in the porosity and the slenderness of cell walls (or ligaments for an open cell foam). For simplicity, in the following discussion at chapter 2, the two types of foams will be referred to as rigid foam and soft foam, respectively. In contrast to the cell walls of rigid foam which partially shares the load after rupture, a fractured cell wall of soft foam merely dangles over the rest of the structure. Such a structural difference induces the dramatic distinction in

energy transmission during fracture. Upon rupture, the remaining elastic energy in a cell wall of rigid foam could be redistributed according to the crack-tip advancement, while that in a slender component could hardly be transferred to its neighbors. The elastic energy in a ruptured slender component is mostly dissipated through local vibration or viscoelastic deformation. As a result, the effective fracture energy would have to include the energy of the entire component rather than just that at the vicinity of the crack faces (i.e. the surface energy).

To better understand this unique mechanism of toughening, one may consider the fracture process of a rubber, in which the crosslinked network of long polymer chains could be regarded as an extreme case of soft foam when each slender ligament shrinks down to a molecular scale. In their classic paper, Lake and Thomas suggest the fracture mechanism of rubber fracture: the energy needed to rupture a polymer chain is much larger than that of a single bond as the entire chain is subject to virtually the same breaking force [11]. After fracture, the broken chains recoil and their entropic elastic energy would not be forwarded to neighboring chains. Thus, the intrinsic fracture energy of rubber scales approximately as $\Gamma_{\text{rubber}} \sim Nn^{\frac{3}{2}} l_{\text{m}} U$, with N being the number of chains per unit volume, n the number of monomers per chain, l_{m} the length of each monomer, and U the energy needed to rupture each monomer [11]. This model has been widely used on rubber, but has seldom been related to the fracture of soft foam. Just by using the analogy, we may also deduce the scaling relation for the fracture energy of soft foam as

$$\Gamma \approx \alpha W_c \psi l \tag{1.1}$$

Here, we use W_c to represent the critical energy density of cell wall at rupture, ψ for the volume fraction (i.e. the relative density) of the solid phase, and l for the characteristic size of the foam (e.g. the height of a cell wall). α is a dimensionless geometric factor. One may arrive at the same result from a different perspective. Due to the special geometry of foam, the sharpness of a crack is always limited by l. The fracture energy is thus given by $\Gamma \sim Wl$ [12], with $W = \psi W_c$ being the effective strain energy density at the crack tip. In the limiting case when the material is stiff enough and the fracture process can be modeled by linear elastic fracture mechanics, by using the effective modulus of the structure $E_{\text{eff}} \sim \psi^2$, this scaling law (1) reduces to the model of stiff foams with the fracture toughness given by $K_{\text{IC}} \sim \sqrt{\Gamma E_{\text{eff}}} \sim \psi^{\frac{3}{2}} \sqrt{l}$ (for open cells) [4]. However, the applicability of the latter, which was derived from linear elastic fracture mechanics by assuming a square-root singularity in the stress field [4], to soft elastic foams undergoing large deformation remains unknown.

It is noteworthy that due to the presence of defects, the rupture strength and thus W_c is usually size dependent, unless the cell walls are thinner than the critical size for theoretical strength. The energy-dissipation mechanism of the soft foam structure, on the other hand, is never limited to microscopic scale. One may refer to a two dimensional macroscopic analogy of soft foam, a net or a netted structure (e.g. a string bag), commonly known for its toughness and notch insensitiveness.

Even though the scaling law (1) seems natural and plausible, it could be hard to verify it directly through experiments. In practice, it is difficult to control the porosity and cell size independently during polymer processing, not to mention the size dependency of W_c. Alternatively, chapter 2 seeks to verify the scaling law through numerical modeling. In the

following sections, a phase-field model for rubber fracture will be adopted to simulate the damage initiation and evolution in hyperelastic cellular structures. The phase-field model for fracture, which is capable of calculating the crack growth according to the energy criterion without a predetermined crack path, is very suitable for structures with complex geometries such as soft elastic foams. The scaling law and the special toughening mechanism will then be demonstrated with the phase-field model. The dependence on the detailed geometry of the foam cells will also be studied.

1.2 Double network composite

Double-network (DN) hydrogels have drawn much attention as a soft material having both high mechanical strength and toughness, while containing up to 90% of water [29]. DN gel consists of two interpenetrating polymer networks: one consisting of relatively short and stiff chains (the 1st network) and the other with much longer and initially coiled chains (the 2nd network). The toughness of a DN gel is orders of magnitude higher than that of a single network gel of either polymer, and is close to that of some biological tissues, such as articular cartilage and connective tissues [30]. The mechanical performances obtained in the optimized double network hydrogel is excellent in both strength and toughness. After solving the brittleness problem of common hydrogels, DN hydrogels substantially extend the potential applications range in smart structures and biomedical engineering [31-33].

Due to excellent performances of DN gels, the mechanical behavior and the toughening mechanism is of great interest to researchers. It is now understood DN gel's increased strength and toughness is due to the following process: energy is dissipated by the large deformation in vicinity of crack tip induces sacrificial breakage of 1st network, while

the intact 2nd network preserves the integrity of the solid structure. The yielding phenomenon is discovered in DN gels, which could also be attributed to the fragmentation of the 1st network [34]. During tensile test, some necking zones form and grow in the DN gel sample and a plateau region appears in the loading curve. The DN gels also show superior extensibility with nearly complete recovery [34]. In addition, a significant hysteresis during the first loading cycle has been found in uniaxial tension and compression loading and unloading experiments for DN gels [35]. While such large hysteresis was never observed for the second loading cycle. This behavior also serves as another evidence for the toughing mechanism of DN gels. It is also believed that the large hysteresis in 1st loading cycle is related to the high toughness of the DN gel.

The classical Lake-Thomas theory predicts the intrinsic fracture energy of polymer scales approximately as $\Gamma_{\text{rubber}} \sim Nn^{\frac{3}{2}} l_{\text{m}} U$, with N being the number of chains per unit volume, n the number of monomers per chain, l_{m} the length of each monomer, and U the energy needed to rupture each monomer [36]. The theory explains the fracture of single network gels very well [37], while for DN gels, is quite different. Brown [38] and Tanaka [39] have independently proposed a similar phenomenological fracture model which suggests by comparing necking zone in uniaxial tension to highly stretched material at crack tip, the energy consumption could be estimated using size of necking hysteresis.

To further understand the superior mechanical properties of a DN gel and to enable quantitative prediction, Wang and Hong's model [40] proposed a phenomenological model for damage evolution and pseudo-elasticity. The model introduced two internal variables to describe two distinct irreversible damage processes in DN gels: the softening due to fracture of the 1st network and the extension of the stretching limit induced by the pullout of the 2nd

network [40]. The model also captured the Mullins effect as well as the stable necking phenomenon of a DN gel under tension, which dissipate a significant amount of energy, and are directly related to the fracture toughness of a DN gel. A mechanistically motivated model has also been developed by integrating the interpenetrating network model and network alteration theory [41].

Inspired by the structure and toughening mechanism of DN gels, a highly stretchable soft composite was designed and fabricated. The experimental samples were made by stacking layers of fabric mesh and VHB acrylic tapes. The two constituents serve the same purpose as the two networks in a DN gel: the stiff but brittle mesh provides the high strength as the 1st network of a DN gel, and the soft but stretchable VHB tape serves as the ductile substrate, just like the 2nd network. The two materials were well-bonded initially, but exhibit significant sliding after the fracture and fragmentation of the mesh, which enables distributed partial damage in the mesh. In this study, the tensile, loading-unloading and crack tolerance properties are investigated for a series of DN composites. A similar necking behavior in DN gel has been found in the tensile tests of DN composites. During tensile loading and unloading test, a significant hysteresis was observed in first loading cycle and second loading cycle attributed to the fracture and sliding of first network fabric mesh. With a preset crack tensile test, fabric mesh break into many small pieces at crack tip to resist facile propagation perpendicular to loading. A 1D shear-lag model will demonstrate that such sliding are the keys to the damage-distribution mechanism of the DN composite. With the optimized components ratio, the DN composite is as strong as the mesh, and at the same time the stretchability is comparable to the VHB tape. With the energy dissipation mechanism similar

to that in the DN gels, the DN composite has a fracture work much higher than either of the base materials.

It is noteworthy that the DN composite itself may be regarded as a macroscopic model for the study of DN hydrogels. On the other hand, it also shows this kind of macro-structure can lead to great enhancement of strength and toughness in composite. Through elucidating the roles of various structural parameters, chapter 3 presents a macrostructure model with optimized structure of DN composite.

1.3 Organization of thesis

The tough network structure materials have recently attracted broad attentions and interests. The main objective of the present study is on the fracture property and toughening mechanism of soft composites. Two types of soft composites will be studied in the following chapters: soft elastic foam and the double-network (DN) composite. In the chapter 2, a theoretical study is carried out over soft elastic foams. By using the analogy between the cellular structure of foams and the network of rubbery polymers, a scaling law for the fracture energy if proposed for soft elastic foams. To verify the scaling law, a phase-field model for the fracture processes in soft elastic structures is developed. The numerical simulations in two-dimensional foam structures of various unit-cell geometries have all achieved good agreement with the scaling law. In addition, the dependences of the macroscopic fracture energy on geometric parameters such as the network connectivity and spatial orientation have also been revealed by the numerical results. Simulations have shown that an effective fracture energy one order of magnitude higher than the base material can be reached by using the soft foam structure.

The chapter 3 presents a combined experimental and theoretical study of the DN soft composite, which consists of stacked layers of fabric mesh and 3M VHB tapes. The composite exhibits a damage evolution process very similar to that in the well-known DN hydrogels. The testing results show that the strength and toughness of the DN composite is highly dependent on the composition, and in certain range, the DN composite exhibits much higher mechanical strength and toughness compared with the base materials. The tensile, loading-unloading and crack tolerance properties are investigated for a series of DN composites. A similar necking behavior in DN gel has been found in the tensile tests of DN composites. During tensile loading and unloading test, a significant hysteresis was observed in first loading cycle and second loading cycle attributed to the fracture and sliding of first network fabric mesh. With a preset crack tensile test, fabric mesh break into many small pieces at crack tip to resist facile propagation perpendicular to loading. To further understand the toughening mechanism of the composite and its relation to DN gels, a 1D shear-lag model I developed to study the damage evolution process. The model suggests the finite sliding over the interface between the mesh and the tape layers serves as the key to the energy dissipation and damage-distribution mechanisms of the DN composite. The model also predicts the stress-stretch relation of the DN composite with various compositions, the results agrees well with experiments. Even though the base materials may not be the best to compose the DN composite, the results demonstrate the possibility of constructing novel macroscopic composites by using the toughening mechanism of DN gels. It is also noteworthy that the DN composite itself may be deemed as a macroscopic model for the study of DN hydrogels.

CHAPTER 2

FRACTURE OF SOFT ELASTIC FOAMS

2.1 Phase-field model of fracture

Numerical simulation of fracture processes has the inherited difficulties in dealing with discontinuities, singularities, and moving boundaries which causes large geometric and even topologic changes. To overcome some of these difficulties, phase-field models of brittle fracture have been developed [1, 13-18, 22]. Recently, phase-field models have also been applied to the brittle fracture of rubbery polymers [23]. Numerical experiments have already shown that these models are capable of capturing both the onset of crack propagation and the damage morphologies of dynamic cracks [19-21]. Without the need to track individual crack or to prescribe a crack path, the phase field method becomes a promising candidate for modeling the fracture of structures with relatively complex geometries, such as the soft elastic foam. The model used in this chapter closely follows these developments, especially those by Karma et al [13] and Hakim and Karma [14].

To describe the state of material damage and to avoid tracking the crack front and faces, a phase field $\phi(\mathbf{X},t)$ varying continuously between the intact region ($\phi=1$) and a fully damaged region ($\phi=0$) is introduced. The loss of integrity in the solid is modeled by writing the elastic strain energy density as a monotonic increasing function of the damage variable, $g(\phi)W_s^0(\mathbf{F})$, where W_s^0 is the strain-energy density of the intact material under the same strain, and g is an interpolation function in the interval $(0,1)$ with vanishing derivatives on both ends. In this study, we choose the interpolant $g(\phi)=4\phi^3-3\phi^4$. As a common practice of hyperelasticity, the deformation gradient tensor $\mathbf{F}$ is used to represent the state of

strain. Following Karma et al. [13], we write the free energy density function to include three contributing terms:

$$W(\phi, \nabla\phi, \mathbf{F}) = g(\phi) W_s^0(\mathbf{F}) + [1 - g(\phi)] W_c + \frac{\kappa}{2} |\nabla\phi|^2 . \tag{2.1}$$

The second term on the right hand side of Eq. (2) represents the energy associated with material damage. When the strain energy at a material particle exceeds the threshold W_c, the damaged state with $\phi = 0$ becomes energetically favorable. Just as in almost all phase-field models, the gradient energy term is added to regulate a smooth transition between the coexisting states. In this chapter, the material constituting the solid phase of the foam is assumed to be isotropic, so that only a scalar coefficient κ is needed for the gradient energy term. In equilibrium, the combination of the second and third terms on the right hand side of Eq. (2) gives the surface energy, i.e. half of the intrinsic fracture energy. The fracture energy of the material modeled by the energy function is approximately $\Gamma \approx 2\sqrt{\kappa W_c}$ [13]. Here, in a body undergoing finite deformation, all energy densities are measured with respect to the volume in the reference state.

Countless number of constitutive models have been developed for hyperelastic solids. Although specific stress-strain relations of the solid phase may affect the ultimate fracture properties of soft foam, such dependence is beyond the scope of the current study. Here for simplicity, we will limit the discussion to a neo-Hookean material of the strain energy function

$$W_s^0(\mathbf{F}) = \frac{\mu}{2}(\mathbf{F} : \mathbf{F} - 3), \tag{2.2}$$

where μ is the initial shear modulus. In contrast to linear elastic solids, rubbery polymers are often modelled as incompressible. To enforce volume incompressibility, approaches such as the application of the Lagrange multiplier are often taken, e.g. by adding to the free energy function a term $-p(\det\mathbf{F}-1)$ with a Lagrange multiplier p representing the pressure field. A physically meaningful model needs to degrade the compressibility simultaneously with the shear stiffness. Directly multiplying the Lagrange multiplier term by $g(\phi)$ obviously does not serve the purpose. Instead, we modify the Lagrange multiplier term slightly by modeling the material as slightly compressible:

$$-pg(\phi)(\det\mathbf{F}-1)-\frac{1}{2}\frac{p^2}{K}. \tag{2.3}$$

By taking the variation of (2.3) with respect to p, one will arrive at an equation of state with a degrading bulk modulus: $p=-g(\phi)K(\det\mathbf{F}-1)$. In the intact state, the large bulk modulus $K>>\mu$ ensures volume conservation; in the fully damaged state, the added term does not affect the field of deformation, and the ad-hoc field p is regulated numerically by the quadratic term in (2.3).

With all the aforementioned energy contributions, the total free energy of the system is simply the volume integral of the energy density, including the terms in (2.3), and the surface integral of the potential of external tractions $\mathbf{t}$:

$$\Pi[\phi,\mathbf{x}]=\int W dV-\int \mathbf{t}\cdot\mathbf{x}dA, \tag{2.4}$$

where $\mathbf{x}(\mathbf{X},t)$ symbolizes the current coordinates of a material particle located at $\mathbf{X}$ in the reference state. The total free energy Π is a functional of the field of damage $\phi(\mathbf{X},t)$ and the field of deformation characterized by $\mathbf{x}(\mathbf{X},t)$. Following Hakim and Karma [14], we neglect

inertia and body forces, and assume the system to be in partial mechanical equilibrium, so that $\delta\Pi/\delta\mathbf{x} = \mathbf{0}$ or

$$\nabla \cdot \mathbf{s} = \mathbf{0}, \tag{2.5}$$

in the bulk, and $\mathbf{N} \cdot \mathbf{s} = \mathbf{t}$ on the surfaces. Here $\mathbf{s} = \partial W/\partial \mathbf{F}$ is the nominal stress, and $\mathbf{N}$ is the unit normal vector on a surface. For the evolution of the phase field ϕ, on the other hand, we assume a linear kinetic law with isotropic mobility m:

$$\dot{\phi} = -m\frac{\delta\Pi}{\delta\phi} = m\left[\kappa\nabla^2\phi - g'(\phi)\left(W_s^0 + p\det\mathbf{F} - W_c\right)\right]. \tag{2.6}$$

To simulate quasi-static fracture processes, a large enough mobility is taken to achieve rate-independent results. Further, to model the irreversibility of fracture processes and to prevent the damaged phase from healing, we force ϕ to be a monotonically decreasing function of time by taking only the positive part of the driving force [22]:

$$\dot{\phi} = -m\left\langle g'(\phi)\left(W_s^0 + p\det\mathbf{F} - W_c\right) - \kappa\nabla^2\phi\right\rangle, \tag{2.7}$$

where the angular brackets indicate an operation of taking the positive values, $\langle\xi\rangle = \left(\xi + |\xi|\right)/2$. Supplemented by proper initial and boundary conditions, Eqs. (2.5) and (2.7) constitute a partial differential system for the coevolution of deformation and damage fields, $\mathbf{x}(\mathbf{X},t)$ and $\phi(\mathbf{X},t)$.

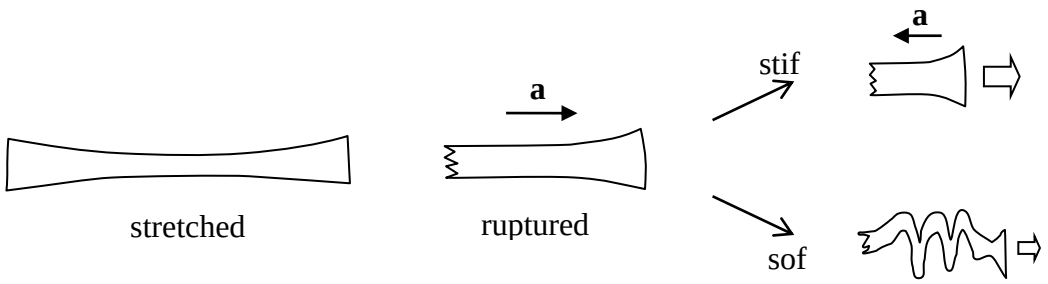

Fig. 2.1 *The rupture and retraction process of a ligament (or cell wall) in a foam structure. Because of its slenderness, a soft filament will tend to buckle or coil and could not effectively transduce energy.*

2.2 Energy dissipation and numerical implementation

The major difference between soft and stiff foams and the primary means of energy dissipation during fracture can be qualitatively understood with the aid of Fig. 2.1. For ease of description, we will refer to the solid dividing segments in both open and closed foams as *ligaments* from now on. Upon rupture from stretched states, a ligament will first be accelerated by its own retracting forces, and the elastic energy stored prior to rupture is mostly converted to kinetic energy. When the ligament retracts further, the difference between stiff and soft ligaments is revealed: while a stiff ligament will remain straight and decelerate and transfer the energy further to the neighboring components, a soft ligament will tend to buckle or coil due to its slenderness, and the energy could not be effectively transferred. The ultimate factor is the stiffness ratio between the surrounding structure and the broken ligament (a buckled ligament has very low stiffness), as elastic wave cannot propagate from a compliant medium to a rigid one. As a result, the elastic energy of a soft ligament is mostly damped through subsequent vibration of itself.

The detailed process and the dependence on the structural geometry, such as the aspect ratio of each ligament and the spatial connectivity at each node, can be simulated by computing the full dynamic response of a ligament and the surrounding structure. Such analysis, however, is not of particular interest to the current study. We will focus on soft foams with very slender ligaments, and hypothesis that most part of the elastic energy stored in the broken ligaments will be dissipated through this process. The results are thus inapplicable to relatively stiff foams. On the other hand, it is also computationally less feasible to model the full dynamic behavior of each ligament in a foam structure of complex geometry. Instead, we will neglect the inertia and model the fracture process as quasi-static. In this limit, the dissipation through crack propagation is negligible, and the fracture energy is mainly dissipated through viscosity. Without considering dynamics, the snap back of the ligaments are fully damped after each rupture event. Instead of a proof or evidence, the calculations presented as follows are the consequence of the proposed energy-dissipation mechanism.

Similar as in many other methods for fracture and damage simulation (e.g. cohesive element and element deletion), without inertia, the damage-induced softening is intrinsically unstable. To stabilize numerical procedures, and more importantly to dissipate the redundant strain energy in the dangling ligaments after rupture, we introduce a Newtonian-fluid-like damping term to the nominal stress

$$\mathbf{s} = \frac{\partial W}{\partial \mathbf{F}} + \frac{\eta}{2}\nabla \dot{\mathbf{x}} \tag{2.8}$$

with η being the numerical viscosity. For relatively small viscosity η, the viscous stress only has significant contribution at the regions of high deformation rate, which is expected to

occur only in a retracting ligament upon rupture. Numerical experiments have shown that when a small value of η is taken, the artificial viscosity only changes the rate of structural unloading at the wake of a propagating crack, and does not affect the energy consumption.

Substituting Eq. (2.8) into (2.5), one may obtain the coevolution of deformation and damage fields by solving the partial differential system (2.5) and (2.7) simultaneously. The system has an intrinsic length scale, $r = \sqrt{\kappa / W_c}$, which is approximately the thickness of the transition zone from the intact region to a full damaged region. It could be argued that r physically characterizes the width of the fracture process zone in the condensed solid phase. Without losing generality, we rewrite the governing equations into a dimensionless form by normalizing all energy densities and stresses by W_c, all lengths by r, and time by $1/mW_c$. After normalization, the dimensionless fracture energy of the solid phase is approximately 2, and the system has only three dimensionless parameters: the normalized shear modulus μ / W_c, bulk modulus K/W_c, and viscosity $m\eta$. In the following numerical examples, we will take dimensionless modulus $\mu / W_c = 0.2$, which corresponds to the representative values of a soft elastomer: $\mu \sim 10\,\text{MPa}$, $r \sim 1\,\mu\text{m}$, and $\Gamma \sim 50\,\text{N/m}$. The dimensionless bulk modulus is taken to be $K/W_c = 200$, and the viscosity $m\eta = 10^{-4}$. It should also be noted that the ligament thicknesses of most structures calculated in the current study are comparable to the intrinsic length scale r. In this limit, the calculations could as well be done by using the regular strength-based material degradation approach. Here, the phase-field approach is taken so that the direct comparison with the fracture process of a bulk material with the same property could be made when needed.

The dimensionless equations are implemented into a finite-element code through the commercial software COMSOL Multiphysics 4.3b. For numerical robustness under large deformation, the geometries are discretized by using triangular elements, and both the displacement and damage fields are interpolated with linear Lagrange shape functions. To capture the transition at the interface between the damaged and intact phases, a maximum mesh size of $0.5r$ is prescribed. The model is integrated over time via a fully coupled implicit scheme, with adaptive step size. To numerically enable damage nucleation, spatial random distributions of the initial shear modulus and the intrinsic fracture energy has been introduced to each model, with standard deviation at 1% of the corresponding magnitudes.

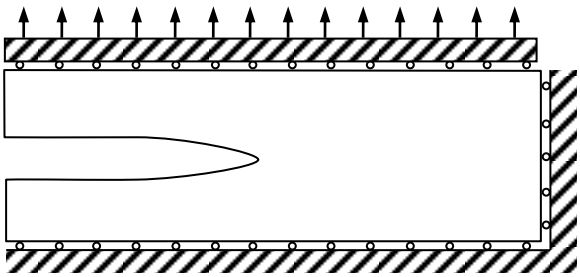

Fig. 2.2. *Sketch of the loading conditions for the foam structures*

To compute the fracture energy, we load the pre-cracked structures in a similar way as the pure-shear test for rubber. As sketched in Fig. 2.2, the right and bottom edges are constrained by rollers, and the top edge is loaded by a uniform displacement. For symmetric structures and if the crack propagates along a symmetry line, only half of the structure is calculated and a symmetry boundary condition is prescribed along the symmetry line. A ramping displacement load is applied within a short time and then held constant. The crack will start to propagate when the applied displacement exceeds certain value. In a steady state when the crack tip is far from either ends, the energy release rate is independent of the crack length,

$$G = W_{\text{eff}} H \,, \tag{2.9}$$

where H is the undeformed height of the structure. W_{eff} is the effective strain-energy density in the absence of the crack, and is averaged over the volume including the space of the pores. In contrast to the standard pure-shear test, the entire structure is under plane-strain condition, and is allowed to shrink horizontally. The corresponding 2D results are closer to the behavior of 3D closed foam. Although the effective strain-energy density W_{eff} can be calculated by integrating W at the region far ahead of the crack tip, here we calculate it separately by subjecting a non-cracked structure to plane-strain uniaxial tension.

2.3 Results and discussion

The simulations are first carried out on hexagonal (honeycomb) structures, as shown schematically in Fig. 3a. In order to reduce boundary effect, the actual computational domain is much larger than that shown. Fillets of dimensionless radius 1 have been applied to all corners to reduce stress concentration, as the preferential damage of the triple junctions may result in a different scaling law. The local deformation and damage fields of a representative result are shown in Fig. 3b, in which the preexisting crack has propagated through three ligaments.

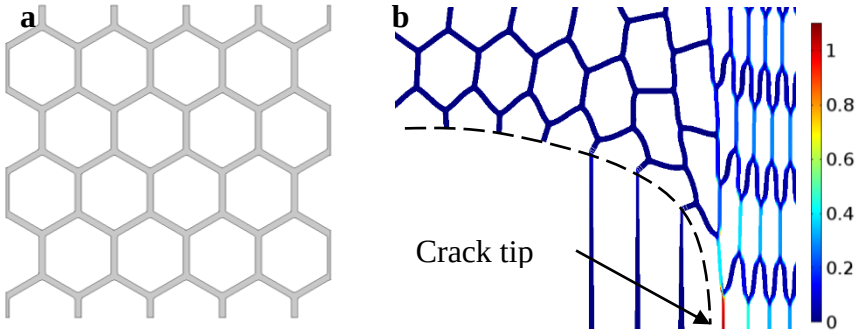

Fig 2.3. *(a) Part of the 2D honeycomb foam structure being simulated. (b) The calculated deformation and damage fields of a honeycomb structure, during the propagation of a preexsting crack. The shades represent the dimensionless strain energy density* W/W_c. *The crack profile is indicated schematically by the dash line, which goes through the the transition zone from the intact to the fully damaged regions in terms of* ϕ. *The deformation is shown to scale, and only part of the structure near the crack tip is shown. The actual computational domain is much larger than that shown to circumvent size-effect.*

In a steady state, a crack is propagating through the structure at a constant speed, the energy release rate G is given by Eq. (2.9). However, due to the discrete nature of the structure, the crack propagation appears staggered. To capture the effective crack velocity, we identify each event of ligament rupture, and record the time of the event and the horizontal coordinate of the corresponding ligament in the undeformed state, as shown by Fig. 2.4a. It is found that when the crack front is far from the edge, the ligament-rupture events are almost equally distributed in time, indicating a steady-state crack propagation. The slope of the linear fit to the rupture events under each loading condition is taken to be the nominal crack velocity v. In consequence of the kinetic law, Eq. (2.6) or (2.7), the energy release rate G, i.e. the driving force of the crack, is rate dependent. As shown by Fig. 4b, the

effective fracture energy of the structure is a monotonic increasing function of the crack velocity. Here, to compare between different structures, we use the threshold value Γ calculated from the vertical intercept of the fracture-energy-velocity curve, as shown by Fig. 4b. The threshold corresponds to the fracture energy of a crack propagating quasi-statically at zero velocity. Following such a procedure, we compute the quasi-static fracture energy of various foam structures, presented as follows.

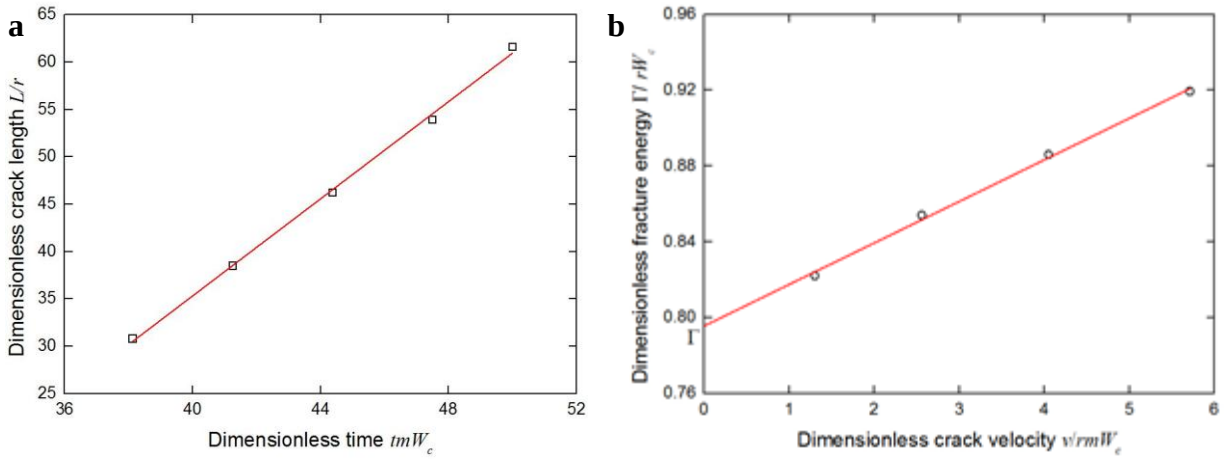

Fig. 2.4. *(a) Undeformed coordinates of the ligaments as a function of the times of rupture. The line is the best linear fit. The slope indicates the dimensionless crack velocity. (b) Dimensionless fracture energy (energy-release rate)* Γ/rW_c *as a function of the dimensionless crack velocity* v/rmW_c *. The line is the best linear fit, and the vertical intercept shows the quasi-static fracture energy of the soft foam.*

The scaling relation (1.1) is verified first through the simulation on the fracture processes of hexagonal soft foams. A set of two-dimensional hexagonal foams of the same volume fraction $\psi = 0.09$ but different ligament lengths are modelled, and their quasi-static fracture energies are computed via the same procedure as described above. The resulting fracture energies of two different orientations are plotted against the ligament length in Fig.

2.5a. In both cases, the dimensionless fracture energy Γ/rW_c is approximately linear in the ligament length l/r. Similarly, we fix the length of each ligament at $l/r = 4.2$, and vary the solid volume fraction from $\psi = 0.025$ to $\psi = 0.17$. The resulting fracture energies of the two orientations are plotted as functions of the solid volume fraction in Fig. 2.5b. As expected, at relatively small volume fraction, the fracture energy is approximately proportional to the volume fraction ψ.

Comparing between the two orientations, it is found that the fracture energy in an "armchair" orientation is consistently higher than that of the same structure in a "zigzag" orientation. Such a difference could be attributed to the anisotropy in ligament density. As illustrated by Fig. 2.6, a horizontal crack mainly goes through the inclined ligaments in the "armchair" orientation, while a crack through a foam in the "zigzag" orientation mainly breaks the vertical ligaments. The numbers of ligaments cut by unit crack length in the two orientations differ by a factor of $2/\sqrt{3}$, which explains the difference in the effective fracture energies. The same phenomena may also be understood by considering the effective sharpness of a crack. As shown by Fig. 2.6, the crack path in a "zigzag" orientation is nearly straight, while that in an "armchair" orientation is often meandering. With the crack front randomly selects one of two inclined ligaments, which has almost identical strain energies, the effective crack tip can be regarded as encompassing the region of both ligaments, and thus the crack is blunter.

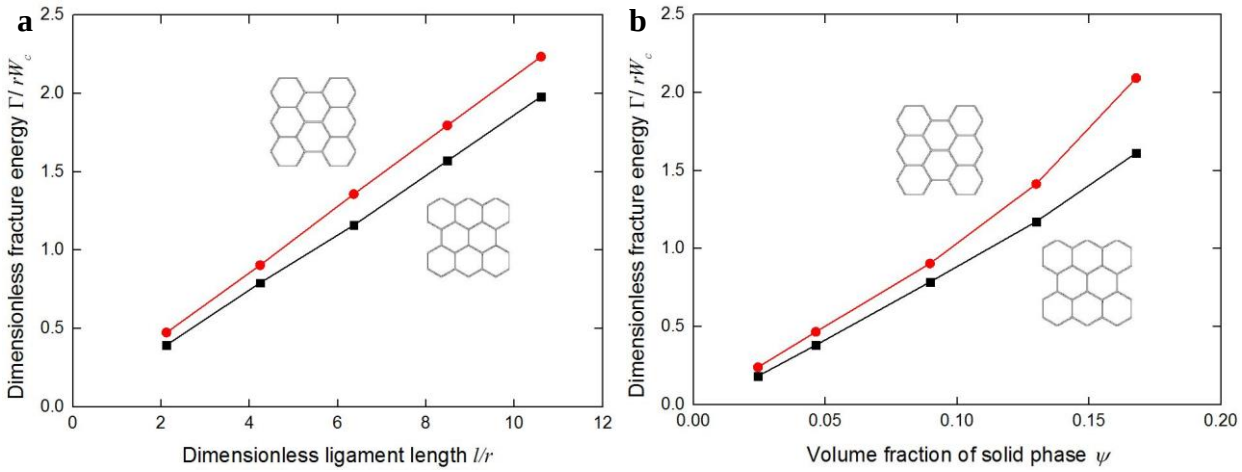

Fig. 2.5. *Calculated fracture energy of the hexagonal soft foams versus (a) the normalized ligament length* l/r *at constant volume fraction* $\psi = 9\%$*, and (b) the volume fraction of the solid phase* ψ *at constant ligament length* $l/r = 4.2$*. Two different orientations are simulated as indicated by the insets (with horizontal cracks).*

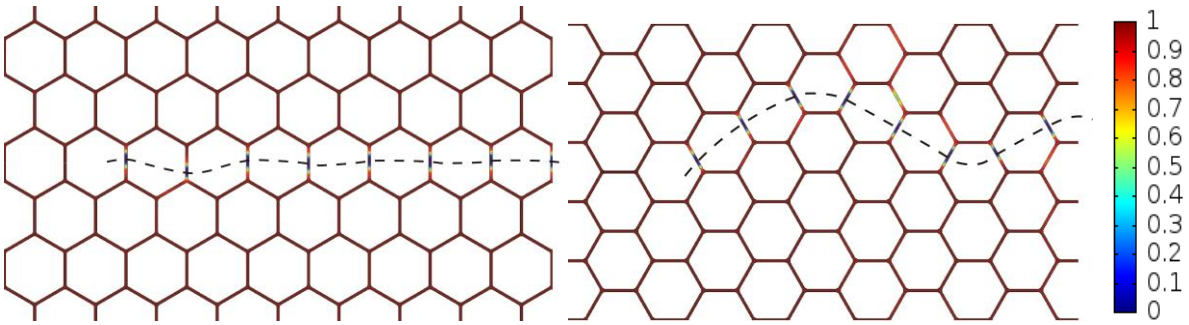

Fig. 2.6. *Damage patterns of hexagonal soft foams in (a) "zigzag" and (b) "armchair" orientations. The color scale represents the damage variable* ϕ*, plotted in the undeformed geometry. The dash curves show the approximate paths of crack propagation.*

The simulations on the crack propagation processes in soft foam structures of various geometries, including those with triangular and square unit cells at different orientations, all exhibit the similar linearity as that observed in the honeycomb foam, which further supports

the scaling relation (1.1). The effect of unit-cell geometry is only reflected in the dimensionless coefficient α, as summarized by Fig. 2.7. Although the relatively high fracture energy of the square-cell foam with vertical/horizontal ligaments may be explained by the higher ligament density than that of the hexagonal foam (one ligament per crack length l versus one ligament per $\sqrt{3}l$ or $2l$), the foams of other patterns do not follow the same trend. Despite the higher ligament densities, the effective fracture energies of the triangular foam or the rotated square foam are actually lower. To understand the relatively low fracture energies, let us revisit the physical origin of the polymer-network-like toughening mechanism. Two necessary conditions must be met for the mechanism to be effective: (a) the ligaments must be relatively long and uniform, so that the elastic strain energy everywhere along a ligament is close to critical prior to rupture; (b) the network structure must be sufficiently compliant, so that the remaining strain energy after rupture is not passed to the neighboring ligaments. Even with the same aspect ratio and uniformity in the ligaments, the network connectivity in either the triangular foam or the square-cell foam is higher than that in the hexagon foam. Each node is connected to six ligaments in a triangular foam, and four in a square-cell foam, but only three ligaments are connected to each node in a hexagonal foam. Therefore, at the tip of a propagating crack in a triangular foam of square-cell foam, two or more ligaments connected to the same node will be stretched and almost aligned in the direction perpendicular to the crack. Once one of them ruptures, the remaining elastic strain energy may be partially transferred through the common node to the other ligaments which are still standing and carrying the load along the same direction. The strain energy carried over may contribute to the further propagation of the crack, and the overall fracture energy is thus lower. It should be noted that the square-cell

foam with vertical and horizontal ligaments represents a special case, in which the two lateral ligaments are connected at the direction almost perpendicular to the load, and thus the macroscopic fracture energy is less affected by the relatively high connectivity.

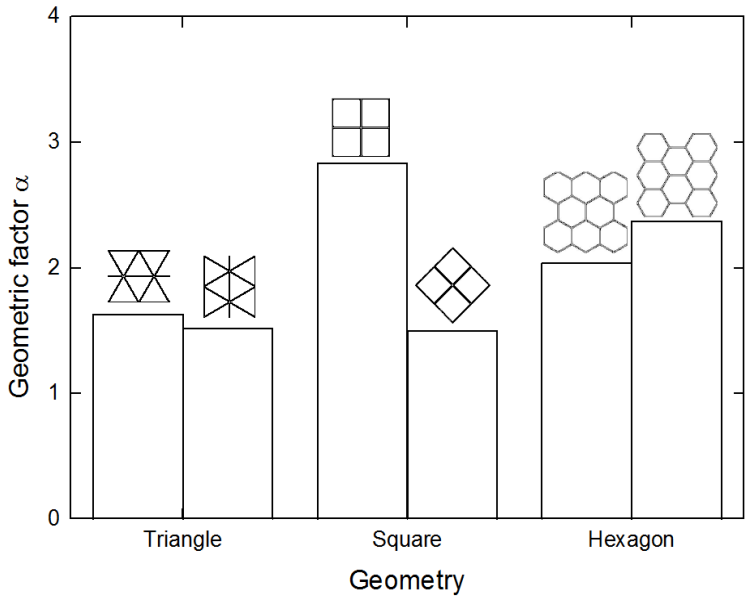

Fig.2.7. *Geometric effect on the fracture energy of soft foams. The geometries and orientations are represented by the sketch insets, with cracks running horizontally.*

Despite the apparent linear relation between the effective fracture energy and the solid volume fraction ψ (or the ligament length l), the polymer-network-like toughening mechanism is unlikely to make a soft cellular material with macroscopic pores tougher than the bulk solid. By using the same method on a bulk solid, we have confirmed that the dimensionless fracture energy of a condensed structure is approximately 2, just as shown in the literature [23]. The factor which has not been taken into consideration here is the size-dependency of material strength. It is well-known that, due to the presence of defects, larger samples of the same material would exhibit a lower tensile strength. The critical energy density W_c which scales with the squared of the rupture strength, is dependent on the

ligament thickness d (and is usually a decreasing function). On the other hand, without resolving microscopic defects, the phase-field model used in the current chapter will not predict any size effect, and W_c is taken as a material parameter for normalization. Instead, if we assume the scaling relation of brittle solids from linear elastic fracture mechanics $W_c \sim d^{-2n}$ with the scaling index $n = 1/2$ [25], and follow the geometric relation for regular closed-cell foams $d \sim \psi l$, we will arrive at an effective fracture energy almost independent of ψ or l. For non-brittle materials, the scaling index n is usually less than $1/2$, and the effective fracture energy will be weakly dependent on ψ and l. Furthermore, in the limiting case when the ligaments are thin enough that the theoretical strength could be achieved, W_c will become size-independent, and the scaling law (1) could be fully recovered. The size-dependency of tensile strength, which has been extensively studied [24], is not a main focus of the current research.

Here we further investigate geometric effects by studying soft elastic foams with non-straight ligaments. The scaling relation, $d \sim \psi l$, represents the geometry of closed-cell foams with relatively straight ligaments (or flat cell walls). In general, if one allows non-straight or folded ligaments, the volume fraction ψ can be varied independently from the ligament thickness d. In other words, one may increase the solid volume fraction ψ while keeping the ligament thickness small to achieve higher fracture toughness in the structure.

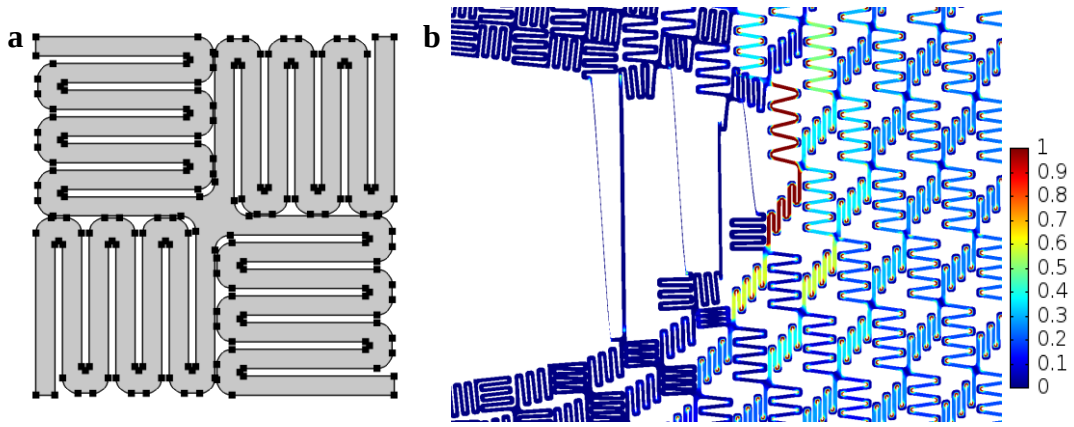

Fig. 2.8. *(a) Sketch of the unit cell of a soft elastic foam containing serpentine ligaments. (b) Simulated deformation and fracture process in the soft elastic foam. The shading shows the dimensionless strain energy density* W/W_c . *The deformed shape is plotted by downscaling the actual displacement value to 10%.*

As an illustrative example, we construct a numerical model by repeating the unit cell as sketched in Fig. 2.8 (a). Unlike in the above examples, the initial geometry of a ligament takes a serpentine form. The material is taken to be soft enough so that the ligaments are insensitive to the stress concentration at the folding corners. During deformation, the ligaments will first be straightened and then rupture. As shown by Fig. 2.8b, the strain-energy distribution in the ligaments at the crack tip is still close to uniform, with the value close to W_c prior to rupture. By varying the width of the serpentine pattern and using the same method as in previous examples, we evaluate the fracture energy of several structures with ligament thickness taken to be r and the unit cell size $18.8r \times 18.8r$, and plot it as a function of the solid volume fraction. As shown by Fig. 2.9., the scaling law (1.1) still holds for the foam structures with serpentine ligaments. Despite the different geometries of the unit cells, the extrapolation of the curve to lower volume fractions will give similar fracture

energy levels as structures with straight ligaments. However, due to the much more condensed nature of the folding structures, the fracture energy is significantly improved. For the structure shown by Fig. 2.8, the volume fraction reaches $\psi \approx 75\%$, and the dimensionless fracture energy is $\Gamma/rW_c \approx 25$, more than one order of magnitude higher than the foam structures with straight ligaments or the same material in a bulk form.

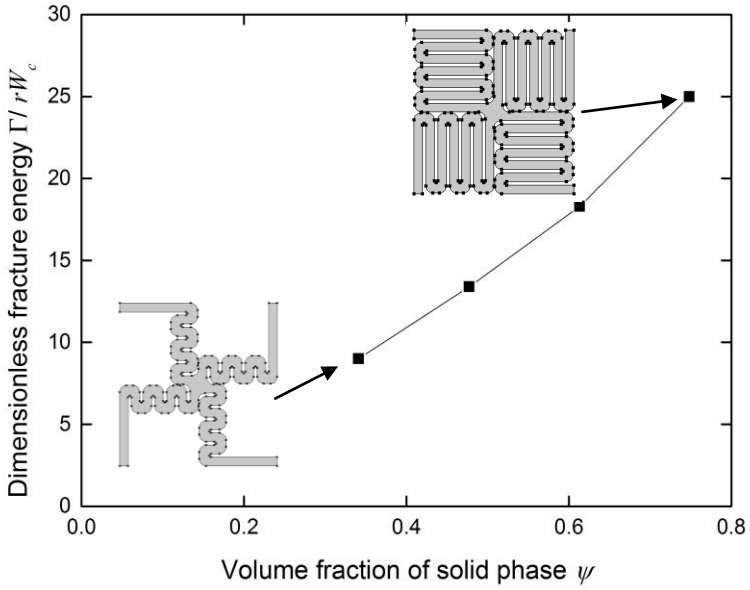

Fig.2.9. *Calculated fracture energy of soft foam structures with serpentine ligaments, as a function of the solid volume fraction* ψ. *The structures have identical unit-cell size and ligament thickness. The volume fraction is controlled by changing the width of the serpentine pattern, as indicated by the insets.*

Without realistic material models or optimized design parameters, this numerical example is just an illustration of the toughening mechanism. Nevertheless, it is evident that the fracture energy of a material may be significantly increased by adopting similar structural designs. More interestingly, such a toughening mechanism is not just limited to soft solids,

especially when the ligament size is small. It should also be noted that the fracture energy increase is obtained at the expense of the initial structural stiffness. As shown by Fig. 2.10., the effective initial modulus is more than two orders of magnitude lower than that of the constituting solid. Such a relation between structural compliance and fracture toughness is similar to that in the microcrack-toughening mechanism, although the latter is usually studied in the context of linear elastic fracture mechanics [26-28].

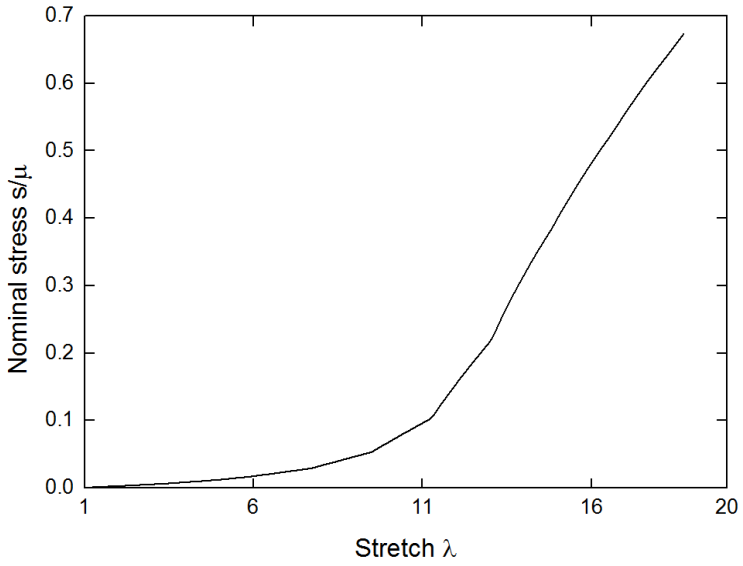

Fig. 2.10. *The calculated nominal-stress-stretch curve of a soft foam with serpentine ligaments as shown by Fig. 8 (without a pre-existing crack). The initial stiffness of the structure is more than two orders of magnitude lower than the solid material. The stress-stretch curve exhibits a strain-stiffening behavior, even though the material is taken to be neo-Hookean.*

Moreover, even though the material is taken to be neo-Hookean, the stress-stretch curve exhibit a clear strain-stiffening segment at relatively large stretch, just like the behavior of elastomers at the stretch limit of polymer chains. Here, the strain stiffening corresponds to

the straightening of the serpentine ligaments. To some extent, such a structure can be regarded as a macroscopic model system for the fracture of elastomers.

The detailed design and optimization of structures of the kind, although interesting, is beyond the scope of the current research. We are eagerly awaiting the designs and manufacturing of tough materials by utilizing this mechanism.

CHAPTER 3

MECHANISM AND FRACTURE OF HIGHLY STRETCHABLE DOUBLE NETWORK COMPOSITE

3.1 Design and fabrication of double network composite

The DN composite samples were prepared by stacking fabric mesh with hexagonal grids alternatingly with VHB acrylic tape 4910 [42], as shown in Fig. 3.1a. The fabric mesh is cut from a roll of Nylon Mandel Fabrics Tulle [43], which is 100 percent Nylon. Owing to the high stickiness of VHB tape, the fabric mesh sticks into the interlayer of two cohesive VHB tapes. The interlayer bonding is due entirely to the adhesion of the VHB tape.

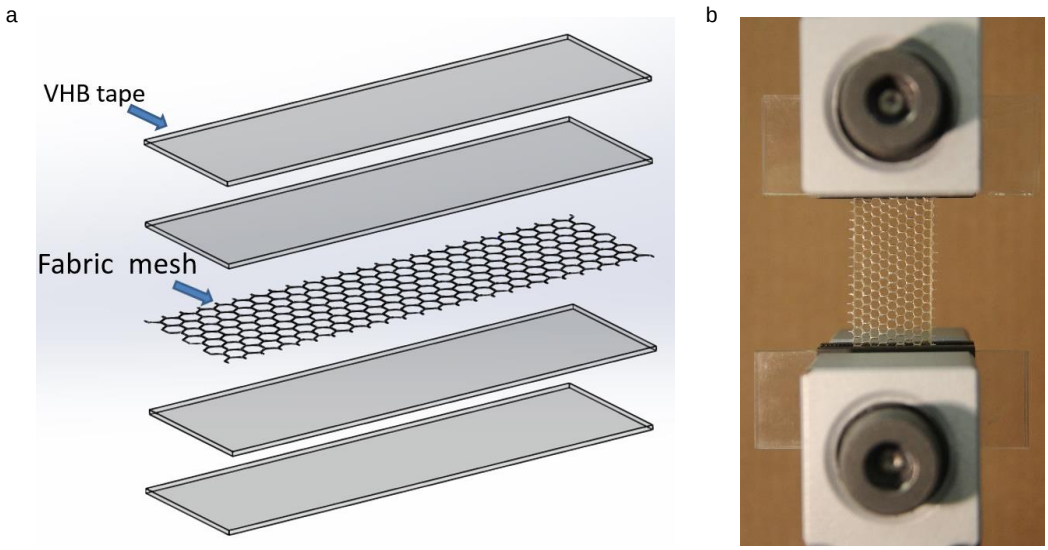

Figure 3.1. *(a) The process of fabricate the DN composite. Stacking nylon fabric mesh with hexagonal grids alternatingly with varying ratios of VHB acrylic tape 4910. (b) Image of a test sample of DN composites.*

The mechanical tests were carried out over an Instron 5960 dual column testing system. Plastic frames are the used to mount the samples before testing, as shown by Fig.1b. Before any

tests on samples, the test methods were run sans sample to check for any vibrations. Since faster extension rates inherently resulted in larger "noise" in the data, several loading rates were tested. By running the same sample type at 15, 30, 60, and 120mm/min, the rate-dependent effect was found to be trivial. The primary test method used was a constant extension rate of 30mm/min and extension distance of 700mm to minimize data noise and have a relatively quick test for different samples while assuring all the samples would break. For the initial tests, a high-speed camera setup was used to capture the predicted "island" formation of the matrix and the fracture behaviors of each sample.

3.2 Experimental results

Tensile tests. In this work, each sample was cut into rectangular shapes of width 25mm and height 50mm (gauge length between grips). As the mesh has negligible thickness compared to the tapes, the sample thickness is approximately the total thickness of the VHB tapes. To get the optimal structure, mesh to VHB tapes ratios of 1:1, 2:3, 1:2, 1:3, 1:4, and 1:5 were fabricated and tested. Here, we use a ½ thinner VHB tape to manufacture the 1:1 sample. The base material: fabric mesh and VHB tape have been also tested.

Figure 3.2 shows typical nominal tensile stress – overall stretch curves of DN composite samples with different composition ratios. The nominal stress was calculated by dividing the force by the original cross-sectional area of the sample. The overall stretch is the deformed sample length divided by initial length. The trend is obvious that the peak nominal stress decreases as the VHB tapes composition increase, while the extension limit increase as the VHB tapes composition increase. The extension limit reaches a plateau when we increase

the VHB tapes from 1:4 sample to 1:5 sample, which is comparable to the extension limit of VHB tape.

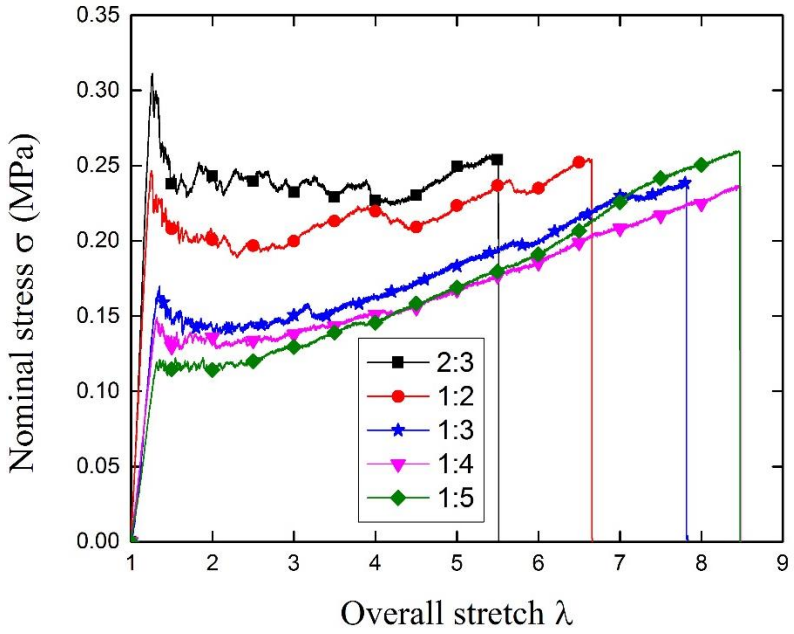

Figure 3.2. *Nominal stress-stretch curve of the DN composite at various compositions, from 2:3 to 1:5.*

Figure 3.3 show a comparison force and overall stretch curve for the representative 1:2 DN composite sample. The DN composite shows excellent extensibility comparable to the VHB tape, which is much larger than that of fabric mesh. As shown by the snapshots C-F in Fig.3a, the DN composite exhibits stable necking during uniaxial tension, just as the DN hydrogels [6]. The necking zone corresponds to the area of partially damaged fabric mesh, as shown by the enlarged picture in Fig.3b. After partial damage in the mesh, the load is carried locally by the much softer tape with large deformation. Due to the ductility of the tape, the subsequent step is the fracture of the mesh in other areas, instead of the rupture of the tape.

Similar as DN hydrogel, the propagation of the partial damage zone (necking) corresponds to the stress plateau on the loading curve, as shown by Fig.3.3a.

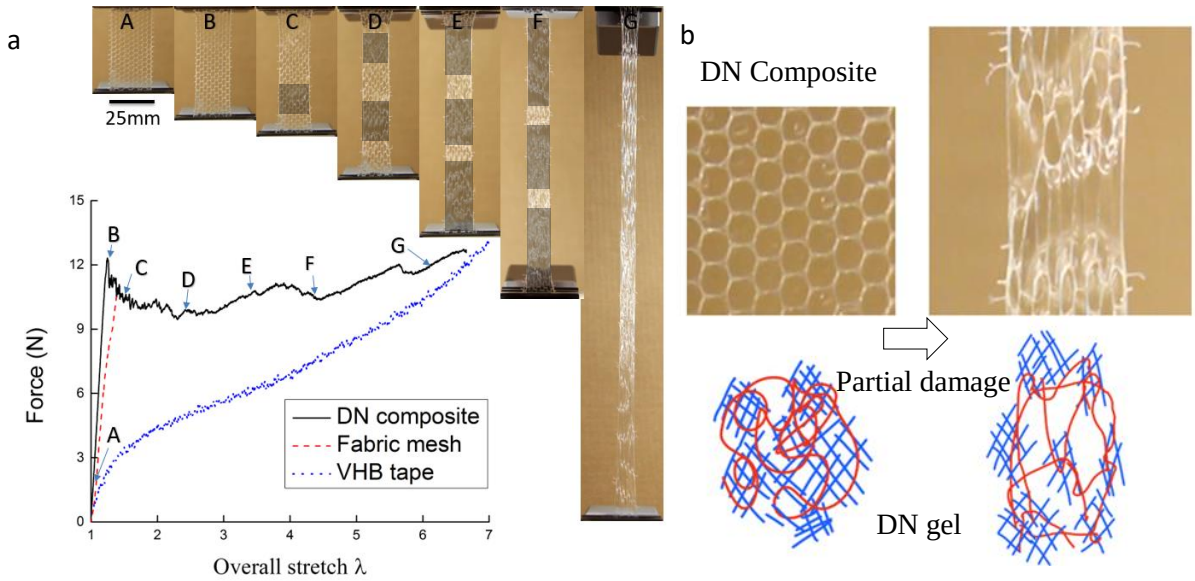

Figure 3.3. *(a) Force-stretch curves of a VHB tape, a fabric mesh, and the DN composite with 1 layer of mesh and 2 layers of VHB tape. For comparison, the force of the VHB tape is multiplied by 2 due to DN composite contains 2 VHB tape layers. The insets A-F are snapshots of the sample correspond to the specific points along the loading curves. The damage zone in C-F stage are marked by the black shaded area. At G stage, the sample is almost damaged everywhere. (b) Comparison between the undamaged and partially damage zones in the DN composite, and a similar mechanism in DN gels.*

Experimental observations also suggested significant sliding between the mesh and the VHB tape in the partially damaged area, as shown in Fig. 3b. The following simple 1D model will demonstrate that such sliding and the consequent non-affine deformation are the keys to the damage-distribution mechanism of the DN composite. It is believed that such a

damage-distribution mechanism is the key to the toughness of the DN composite as well as the DN gels [2].

Loading-unloading test. We also perform the tension loading and unloading test for the sample with the same sample size in tensile test. Here, we use a 1:2 (mesh to VHB tapes ratio) sample as a representative sample. We observed a significant hysteresis during the first loading cycle and second loading cycle. Fig. 3.4 shows subsequent cycles of nominal tensile stress- stretch curves. For 1st cycle, the stress increased strongly at first and reaches the peak stress. While for 2nd cycle, the stress increases slowly compared with the 1st cycle, which is corresponding to softening effect of DN composite due to the partial damage of mesh in the sample. Finally, the sample breaks in the 3rd cycle. Here the difference between the stress of unloading region and that of loading region in the following cycle also serves as an evidence for the sliding behavior between the mesh and the VHB tape.

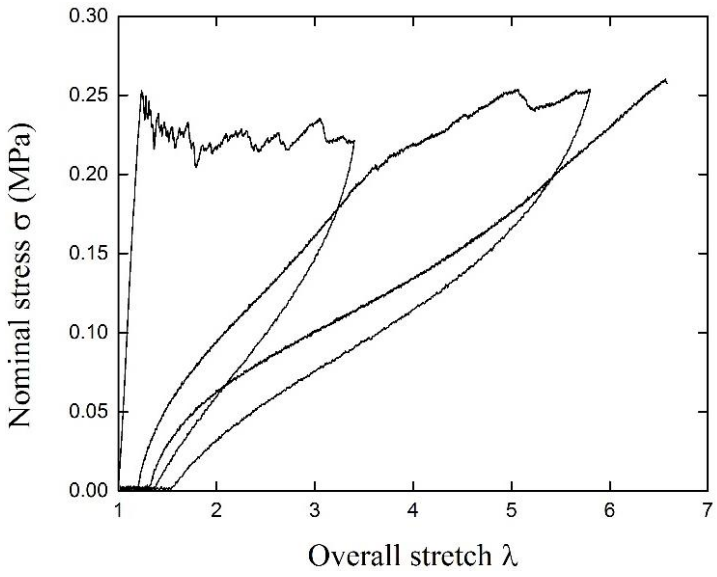

Figure 3.4. *Loading and unloading curves for one 1:2 DN composite.*

Preset crack test. To test the crack tolerance behavior of DN composite, a preset 30mm crack is cut on one side of the specimen with the dimension of 100 mm x 100 mm. The fabric mesh, VHB tape and DN composites with different composition ratios from 1:2 to 1:6 were fabricated and tested.

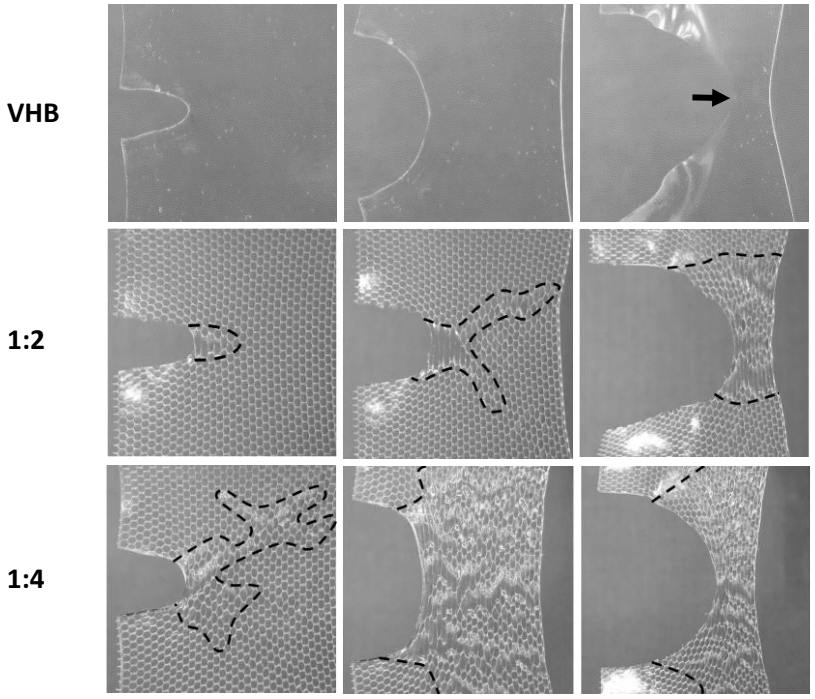

Figure 3.5. *Illustration of local damage zone at damage zone at the crack front of DN composites. Three different samples are selected, which are VHB sample, 1:2 and 1:4 DN composites. The process zone for each DN composite is marked by the black dash line. For each sample, the 1st snapshot is the initial stage under the same stretch. The 2nd snapshot is the moment after which the crack starts to propagate. The 3rd snapshot is captured during the crack propagation.*

From experimental observations in Fig. 3.5, the crack propagation process can be divided into two stages. First, the fabric mesh failure at very small stretch, and it break into

many small pieces at crack tip before the VHB tape crack propagated. Several damaged zones around the crack tip are bridged by the VHB tape and the DN composite remains continuous. The second stage of failure involves crack propagation in the VHB tape. The damaged region around crack tip is the process zone where the fabric mesh has been broken up. As the number of VHB layers increase, the process zone size increases, which can be seen in Fig.3.5b. The process zone size in 1:4 sample is much larger than that in 1:2 sample. In addition, the 1:4, 1:5 and 1:6 DN composite samples almost have whole region before the crack tip damaged.

The force-stretch curve and nominal stress-stretch curve are plotted in Fig. 3.6. From the force-stretch curve in Fig. 3.6a we can clearly see the extension limit of the DN composite with one layer of fabric mesh increase significantly compared with the fabric mesh. In addition, the nominal stress-stretch curve in Fig. 3.6b shows the strength of the VHB tape can be enhanced by making it to the DN composites. To compare the toughness for all the samples with different layer ratio, we calculate the fracture work for each sample and plotted it in Fig. 3.7. The results show the DN composites are much tougher than the VHB tapes and also the optimal layer ratio is 1 fabric mesh with 4 layer of VHB tapes.

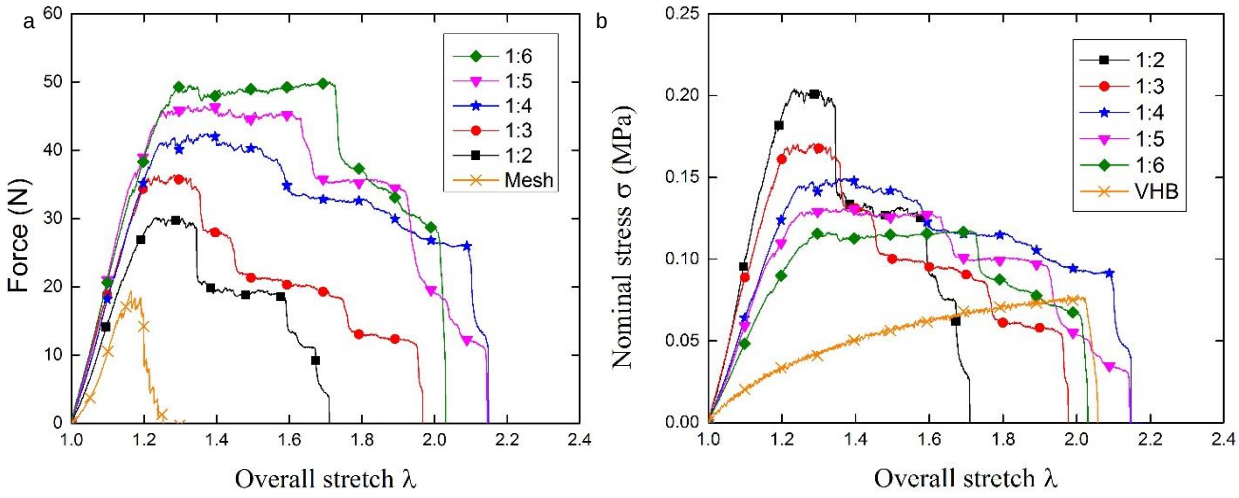

Figure 3.6. *(a) Force-stretch curve for crack tolerance test of the DN composite at various compositions and mesh only. (b) Nominal stress-stretch curve for crack tolerance test of the DN composite at various compositions and VHB tapes only.*

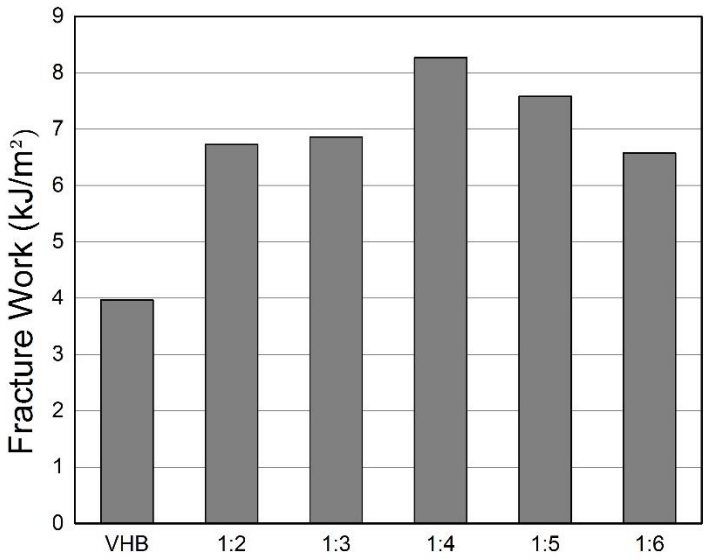

Figure 3.7. *Fracture work of VHB tape and DN composites with different ratios.*

By comparing the nominal stress-stretch curves of preset crack samples and those of intact samples, we found the damage tolerance behavior of DN composites is very good. For the optimal layer ratio 1:4 sample, the peak stress for preset crack sample is almost the same with the intact sample, which gives equal strength for damaged sample. In addition, the optimal layer ratio agrees with the best one in tensile test.

3.3 Modeling results and discussion

We propose a simple shear-lag model to measure the strength of the DN composite. Consider a partially damaged state of the composite, which corresponds to a point on the plateau of the stress-strain curve. The mesh is fragmented into discontinuous islands, while

the underlying VHB tape is still one piece, with the sliding indicated by the sliding traces in Fig.8. The interaction between the mesh and the tape, as well as the stress and force distribution in each layer, are illustrated in Fig. 3.8. A relatively large island of the fragmented mesh can be divided into three regions along the direction of the load. On both sides, two relatively large regions (B and D on Fig. 3.8) exhibiting interlayer sliding are present, and a center region (C on Fig.3.8) where the mesh and the tape deform coherently. The characteristic sizes of the two regions are denoted by L and r in the *deformed* configuration. In general, there should be a transition zone between the two regions which scales with the thickness of the tape. In the current research, the effect of the transition zone will be neglected and the deformation in both layers will be assumed to be uniaxial. It is noteworthy that the membrane force f is defined as a homogenized quantity in the mesh layer, averaged over a region larger than the mesh grid.

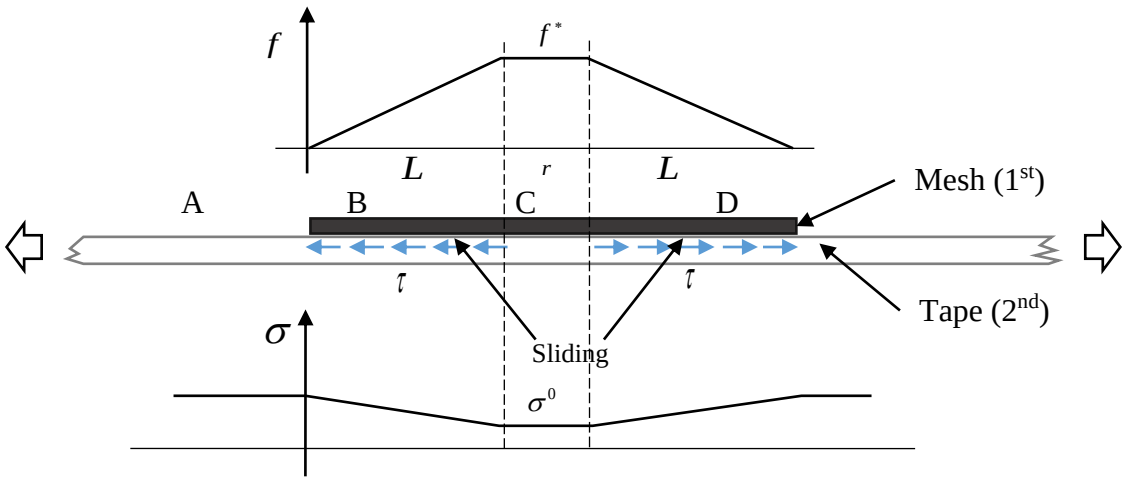

Figure 3.8. *The interaction between the mesh and the tape. The force distribution in the mesh and stress distribution in the tape.*

Due to the sliding, a shear stress is present between the mesh and the tape, which transfers the axial load gradually between the two layers, as sketched in Fig. 8. Here for simplicity, we approximate this interaction by a shear-lag model with constant shear stress τ in the deformed configuration. Under such an assumption, the resulting axial stress and force distributions in the mesh and the tape are qualitatively shown by Fig. 8. The stress in the tape maximizes in zone A where bare tape is exposed due to sliding, and the membrane force in the mesh is maximized in the middle of each island, zone C. For effective energy dissipation, it is essential to have the partially damaged mesh (the 1st network) to fragment further rather than the tape (the 2nd network) fracture right under an existing crack of the mesh. Therefore, the force in the mesh at zone C should reach the tensile strength f^*, while that in the tape at zone A should be below the strength of the tape $\sigma < s_{2\text{nd}}$. Such a requirement sets the size of the sliding zone (B and D) in a steady state,

$$L \approx \frac{f^*}{\tau}. \tag{3.1}$$

The fragmentation will continue until the size of the middle zone r becomes comparable or smaller than the intrinsic fracture process zone size, $r_{1\text{st}}$, below which the rupture of the material is insensitive to stress concentration and the effective strength significantly increases. Here, the intrinsic fracture process zone is approximately the mesh size.

Let us first consider the deformation in the mesh layer. From the testing results on the bare mesh, we assume it to be linearly elastic, with the membrane force f proportional to the strain ε:

$$f = k\varepsilon, \tag{3.2}$$

where k is the effective tensile stiffness of the mesh. In zone C, when the mesh is in a critical state and the island is about to further fragment into smaller ones, $f = f^*$, the deformed width r is related to the undeformed one r_0 by $r = r_0\left(1+ f^*/k\right)$.

In the sliding zone B, the lateral force balance of the mesh layer dictates a linear distribution of the membrane force:

$$f = \tau x . \tag{3.3}$$

Utilizing (3.2) and (3.3) and considering (3.1), we obtain the relation between the deformed length L and the corresponding length before deformation L_0:

$$\frac{L}{L_0} = 1 + \frac{f^*}{2k} . \tag{3.4}$$

Now let us turn to the deformation in the VHB tape. Due to the finite sliding, the part of the tape that was beneath the mesh island becomes much longer. Denote the total deformed length of the sliding segment by l. The horizontal equilibrium of the tape gives the stress distribution

$$\sigma = \begin{cases} \sigma^0 + \dfrac{\tau L}{H} & (L - l < x < 0) \\ \sigma^0 + \dfrac{\tau}{H}(L - x) & (0 < x < L) \end{cases}, \tag{3.5}$$

where σ^0 is the stress in the non-sliding segment C, and H the original thickness of the tape. In the absence of relative sliding, the strain in the VHB tape in zone C matches with that in the mesh, and σ^0 is the corresponding axial stress. When a certain constitutive model for the VHB tape selected, and the stress-stretch relation $\sigma(\lambda)$ is prescribed, Eq. (3.5) can be used to determine the deformation field in the tape layer. Here by referring to the test result

of the VHB tape, we select the incompressible neo-Hookean model. The uniaxial stress is related to stretch as

$$\sigma = \mu\left(\lambda - \frac{1}{\lambda^2}\right), \tag{3.6}$$

where μ is the initial shear modulus. When the mesh in zone C reaches the critical point, $f = f^*$, the stress in the underlying tape layer is

$$\sigma^0 = \mu\left(\lambda^* - \frac{1}{\lambda^{*2}}\right), \tag{3.7}$$

where $\lambda^* = r/r_0 = 1 + f^*/k$.

By integrating the inverse of stretch over the deformed length of the sliding zone on the tape, a relation between its original length L_0 and the deformed length l can be obtained:

$$L_0 = \int_{L-l}^{L} \frac{dx}{\lambda}. \tag{3.8}$$

The integral can be evaluated numerically with the stretch values obtained from Eqs. (3.5-3.7). The system has two dimensionless parameters: the stretch at fracture of the mesh $\lambda^* = 1 + f^*/k$, and the ratio between the strength of the mesh and the stiffness of the tape $f^*/\mu H$. Just as the first network in the DN gel, the mesh provides the overall stiffness of the composite and acts as the sacrificial component. With limited stretchability, the range of the critical stretch λ^* is relatively small and is thus not a major contributor to the toughness of the composite. Here we take the representative value from the experimental measurements (Fig. 3), $\lambda^* = 1.1$. On the other hand, the strength-stiffness ratio $f^*/\mu H$ plays an important role in the stretchability and toughness of the composite. Here through

integrating (3.8) numerically, we plot the average stretch l/L_0 in the sliding zone of the VHB tape as a function of the dimensionless parameter $f^*/\mu H$ in Fig. 3.9.

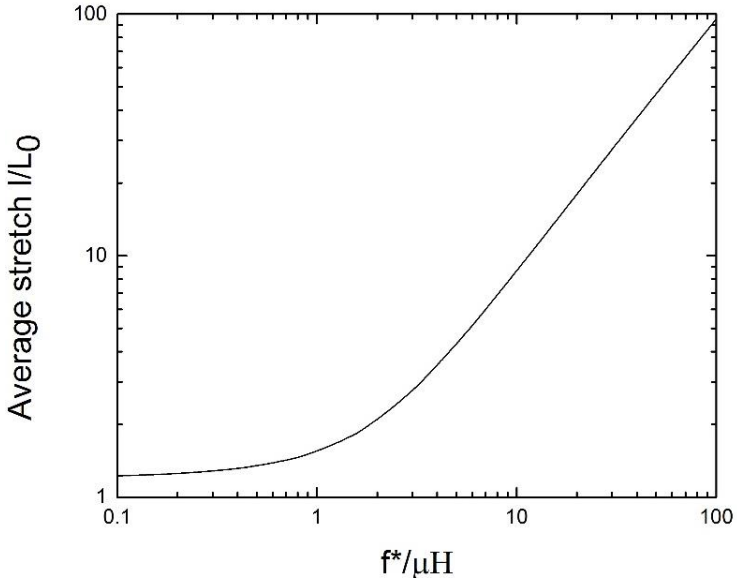

Figure 3.9. *The average stretch in the sliding segment of the tape, plotted as a function of the ratio between the strength of the mesh and the stiffness of the tape,* $f^*/\mu H$.

Over the stress plateau, subdivide larger islands into smaller ones will take place until each island is too small to be subdivided, i.e. the half-size of the island becomes smaller than f^*/τ. For a smaller island, the axial force accumulated from the shear lag can no longer reach f^*. In those islands, the non-sliding zone r shrinks to 0, and thus the stretches in the two layers do not need to match. The stress in the tape σ^0 is no longer determined by Eq. (3.7) and would keep increasing until the tape layer ruptures. The cessation of the island-fragmentation mechanism corresponds to the end point of the plateau on the stress-strain curve. In the absence of the non-sliding zones, the overall stretch of this point is given by

$\lambda_{\text{lim}} \approx l/L_0$. As shown by Fig. 3.10, for relatively large $f^*/\mu H$, l/L_0 simply scales linearly with it. We thus arrive at the approximate scaling law for the limiting stretch of the plateau:

$$\lambda_{\text{lim}} \approx \frac{f^*}{\mu H}. \tag{3.9}$$

By using the model presented above, the effective stress-stretch curve of the composite can be reconstructed theoretically. The deformation and damage process of the DN composite can be divided into three stages. In stage I, before any damage, the behavior of the composite is close to linear elastic, with the effective stress

$$\sigma \approx \left(\frac{k}{H} + 3\mu\right)(\lambda - 1). \tag{3.10}$$

By writing Eq. (3.10), the thickness of the mesh layer is neglected and the thickness of the composite is assumed to be identical to that of the constituting VHB tapes. At a critical stretch, λ^*, the partial damage in the mesh initiates. Upon further stretch, the deformation is manifested through the further fragmentation of the mesh (or the propagation of the damage to the undamaged region when necking is present). In stage II, the stress is maintained at a level close to that of fracturing the mesh:

$$s \approx \frac{f^*}{H}\left(1 + \frac{3\mu H}{k}\right). \tag{3.11a}$$

The stress plateau extends all the way to a stretch $\lambda_{\text{lim}} \approx f^*/\mu H$, beyond which the stress will increase again. The monotonic increasing curve in stage III is mainly governed by the behavior of the tape layer, and the stress is bounded by a value set by the strength of the tape: $s_{2\text{nd}}$. While the accurate stress-stretch relation can be obtained by numerically solve Eqs. (3.5) and (3.6) and integrating Eq. (3.7), for relatively small range of deformation, the

behavior is close to linear. The behavior in stage III can be approximately characterized by shifting the stress-stretch curve of the VHB tape up to the point $(\lambda_{\text{lim}}, s)$.

We take the values measured from independent experiments on the mesh and tape individually: $k = 1170\ \text{Nm}^{-1}$, $f^* = 420\ \text{Nm}^{-1}$, and $\mu = 38\ \text{kPa}$, calculate the stress-stretch relation numerically from the model, and plotted in Fig. 3.10. Comparing to the experiment results in Fig. 3.2, the agreement between the shear lag model and experiments is reasonably well.

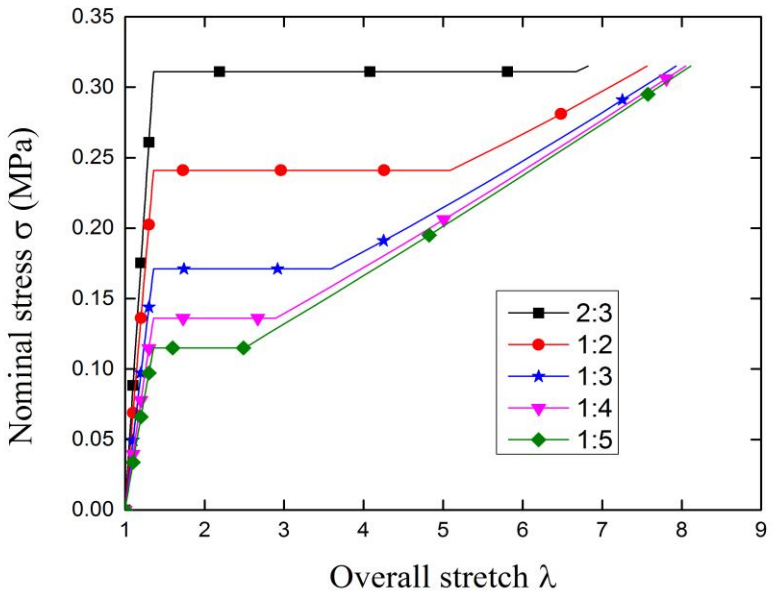

Figure 3.10. *Theoretical prediction by considering the interaction in the sliding zone with a shear-lag model. The five curves have the same mesh to VHB tape ration as Fig. 3.2, which are 2:3 to 1:5. Material parameters are extracted from independent experiments on base materials.*

We can reconstruct Eq.11a to the following equation,

$$s \approx f^* \cdot \frac{1}{H} + \frac{3\mu f^*}{k}. \tag{3.11B}$$

The peak stress and plateau stress during the tensile test of DN composites is plotted versus 1/*H* as in Fig. 3.11. The agreement in peak stress between the shear lag model and experiments is also very well comparing to the experiment results.

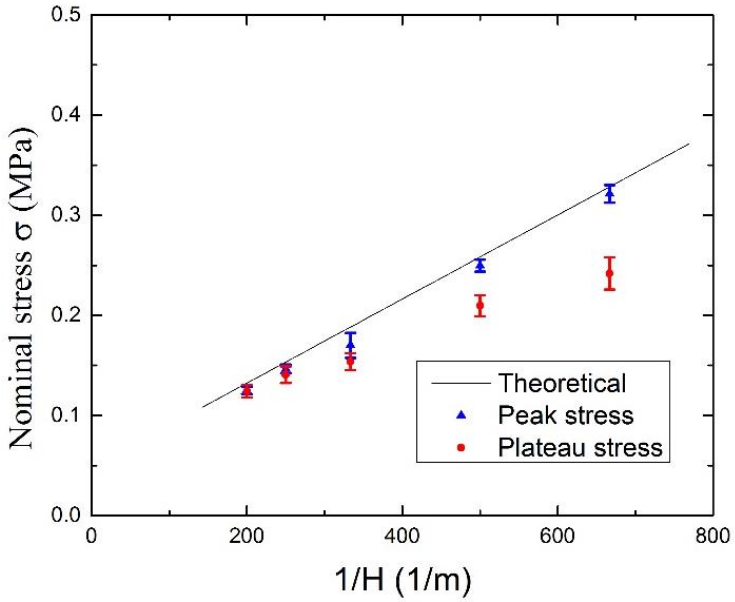

Figure 3.11. *Theoretical peak stress, experimental peak stress and experimental plateau stress versus 1/H.*

If the sample is unloaded from a point in Stage II, the unloading curve is approximately the weighted average between the undamaged and damaged behavior. If the effect of the sliding stress τ is negligible, the behavior of the fully damaged material will be close to that of the tape. The unloading stress is thus given by

$$\sigma \approx \phi\left(\frac{k}{H}+3\mu\right)(\lambda-1)+(1-\phi)\mu\left(\lambda-\frac{1}{\lambda^2}\right), \tag{3.12}$$

where ϕ is the volume fraction of the undamaged phase, and can be easily determined from the stretch at the onset of the unloading, where the stress equals the plateau value s. Without the friction from sliding, the unloading and reloading curves coincide with each other. However, testing results show a small hysteresis between the unloading and reloading curves, as in Fig. 3.4. This, in turn, could serve as the evidence of the sliding, and the size of the hysteresis may be used to estimate the sliding stress τ. Such a practice, however, is beyond the scope of the current study.

While the presence of the sliding between the mesh and the tape is essential to the energy dissipation in the damage process, according to the simple model, the actual value of the sliding stress τ does not affect the ultimate stretch or the resulting toughness of the composite. However, a smaller sliding stress will lead to a larger sliding area, and thus the approximate which corresponds to the extreme case when $r_0 << L_0$ will be more accurate.

CHAPTER IV

CONCLUSIONS

Drawing an analogy between the compliant ligaments in a soft elastic foam and the polymer chains in an elastomer, chapter 2 proposes a polymer-network-like toughening mechanism and derives the scaling relation between the macroscopic fracture energy and the structural characteristics of soft foam structures. Different from the energy absorbing mechanism of rigid foams which is mainly effective at compression, the polymer-network-like toughening mechanism allows a soft foam to effectively dissipate energy when the structure is subject to tension. Through a phase-field model developed specifically for the fracture of elastomers, the toughening mechanism as well as the scaling relation is then verified on soft foam structures of various geometries. In addition to the scaling law, it is found that the geometric parameters such as the ligament density and the network connectivity will also affect the fracture energy of soft foams. Finally, to increase the volume fraction of the solid phase without affecting the thickness or slenderness of each ligament, a type of soft foam structures of serpentine ligaments is proposed. Numerical study suggests that such structures may reach an effective fracture energy much higher than that of the corresponding bulk material. In other words, one may toughen a soft material just by cutting slots or holes in it. In chapter 3, using a fabric mesh and a VHB acrylic tape, a soft but highly stretchable DN composite is manufactured. The DN composite follows the same damage-distribution and toughening mechanisms as in the well-known DN hydrogels. The DN composite exhibits stable necking as the DN gel, possesses large hysteresis during tensile loading-unloading test and shows good crack tolerance. The DN composite is as strong as the

mesh, as stretchable as the tape, and much tougher than both materials. By using a simple shear lag model to capture the finite interlayer sliding, a theory is developed and its prediction in the stress-strain behavior agrees well with the experiments. On the other hand, the DN composite itself may be regarded as a macroscopic model for the study of DN hydrogels. It also provides another kind of macro-structure composite which can lead to great enhancement of strength and toughness.

REFERENCES

[1] Aranson, I. S., Kalatsky, V. A., & Vinokur, V. M., 2000, “Continuum field description of crack propagation,” Physical review letters, **85**(1), 118.

[2] Maiti, S. K., Gibson, L. J., & Ashby, M. F., 1984, “Deformation and energy absorption diagrams for cellular solids,” Acta metallurgica, **32**(11), pp. 1963-1975.

[3] Han, F., Zhu, Z., & Gao, J., 1998, “Compressive deformation and energy absorbing characteristic of foamed aluminum,” Metallurgical and Materials Transactions A, **29**(10), pp. 2497-2502.

[4] Gibson, L. J., & Ashby, M. F., 1999, “Cellular solids: structure and properties,” Cambridge university press.

[5] Maiti, S. K., Ashby, M. F., & Gibson, L. J., 1984b, “Fracture toughness of brittle cellular solids,” Scripta Metallurgica, 18(3), pp. 213-217.

[6] Gibson, L. J., Ashby, M. F., Zhang, J., & Triantafillou, T. C., 1989, "Failure surfaces for cellular materials under multiaxial loads—I. Modelling,” International Journal of Mechanical Sciences, 31(9), pp. 635-663.

[7] Brezny, R., & Green, D. J., 1991, “Factors controlling the fracture resistance of brittle cellular materials,” Journal of the American Ceramic Society, 74(5), pp. 1061-1065.

[8] Chen, J. Y., Huang, Y., & Ortiz, M., 1998, “Fracture analysis of cellular materials: a strain gradient model,” Journal of the Mechanics and Physics of Solids, 46(5), pp. 789-828.

[9] Bažant, Z. P., Zhou, Y., Zi, G., & Daniel, I. M., 2003, “Size effect and asymptotic matching analysis of fracture of closed-cell polymeric foam,” International journal of solids and structures, 40(25), pp. 7197-7217.

[10] McIntyre, A., & Anderton, G. E., 1979, "Fracture properties of a rigid polyurethane foam over a range of densities," Polymer, 20(2), pp. 247-253.

[11] Lake, G. J., & Thomas, A. G., 1967, "The strength of highly elastic materials," Proceedings of the Royal Society of London, Series A, Mathematical and Physical Sciences, 300(1460), pp. 108-119.

[12] Thomas, A. G., 1955, "Rupture of rubber. II. The strain concentration at an incision," Journal of Polymer science, 18(88), pp. 177-188.

[13] Karma, A., Kessler, D. A., & Levine, H. (2001), "Phase-field model of mode III dynamic fracture," Physical Review Letters, 87(4), p. 045501.

[14] Hakim, V., & Karma, A., 2009, "Laws of crack motion and phase-field models of fracture," Journal of the Mechanics and Physics of Solids, 57(2), pp. 342-368.

[15] Eastgate, L. O., Sethna, J. P., Rauscher, M., Cretegny, T., Chen, C. S., & Myers, C. R., 2002, "Fracture in mode I using a conserved phase-field model," Physical Review E, 65(3), p. 036117.

[16] Wang, Y. U., Jin, Y. M., & Khachaturyan, A. G., 2002, "Phase field microelasticity theory and modeling of elastically and structurally inhomogeneous solid," Journal of Applied Physics, 92(3), pp. 1351-1360.

[17] Marconi, V. I., & Jagla, E. A., 2005, "Diffuse interface approach to brittle fracture," Physical Review E, 71(3), p. 036110.

[18] Spatschek, R., Hartmann, M., Brener, E., Müller-Krumbhaar, H., & Kassner, K., 2006, "Phase field modeling of fast crack propagation," Physical review letters, 96(1), p. 015502.

[19] Karma, A., & Lobkovsky, A. E., 2004, "Unsteady crack motion and branching in a phase-field model of brittle fracture," Physical review letters, 92(24), p. 245510.

[20] Henry, H., & Levine, H., 2004, “Dynamic instabilities of fracture under biaxial strain using a phase field model,” Physical review letters, 93(10), p. 105504.

[21] Henry, H., 2008, “Study of the branching instability using a phase field model of inplane crack propagation,” EPL Europhysics Letters, 83(1), p. 16004.

[22] Miehe, C., Welschinger, F., & Hofacker, M., 2010, “Thermodynamically consistent phase-field models of fracture: Variational principles and multi-field FE implementations,” International Journal for Numerical Methods in Engineering, 83(10), pp. 1273-1311.

[23] Miehe, C., & Schänzel, L. M., 2014, “Phase field modeling of fracture in rubbery polymers. Part I: Finite elasticity coupled with brittle failure,” Journal of the Mechanics and Physics of Solids, 65, pp. 93-113.

[24] Bazant, Zdenek P, “Scaling of structural strength,” Butterworth-Heinemann, 2005.

[25] Griffith, A. A. “The Phenomena of Rupture and Flow in Solids,” Philosophical Transactions of the Royal Society (London), 221 (1921), pp. 163–198.

[26] Hoagland, R. G., Embury, J. D., and Green, D. J.. "On the density of microcracks formed during the fracture of ceramics." Scripta Metallurgica 9, no. 9 (1975): 907-909.

[27] Evans, A. G. and Fu, Y.. "Some effects of microcracks on the mechanical properties of brittle solids—II. Microcrack toughening." Acta Metallurgica 33, no. 8 (1985): 1525-1531.

[28] Hutchinson, J. W.. "Crack tip shielding by micro-cracking in brittle solids." Acta metallurgica 35, no. 7 (1987): 1605-1619.

[29] Gong, J.P., Katsuyama, Y., Kurokawa, T. and Osada, Y., 2003. Double-network hydrogels with extremely high mechanical strength. Advanced Materials, 15(14), pp.1155-1158.

[30] Gong, J.P., 2010. Why are double network hydrogels so tough? Soft Matter, 6(12), pp.2583-2590.

[31] C. Azuma, K. Yasuda, Y. Tanabe, H. Taniguro, F. Kanaya, A. Nakayama, Y. M. Chen, J. P. Gong and Y. Osada, J. Biomed. Mater. Res., Part A, 2006, 81, 373.

[32] B. J. DeKosky, N. H. Dormer, G. C. Ingalve, C. H. Roatch, J. Lomakin, M. S. Detamore and S. H. Gehrke, Tissue Eng., Part C, 2010, 16, 1533.

[33] A. Rakovsky, D. Marbach, N. Lotan and Y. Lanir, J. Appl. Polym. Sci., 2009, 112, 390.

[34] Na, Y. H., Tanaka, Y., Kawauchi, Y., Furukawa, H., Sumiyoshi, T., Gong, J. P., & Osada, Y. (2006). Necking phenomenon of double-network gels. Macromolecules, 39(14), 4641-4645.

[35] Webber, R. E., Creton, C., Brown, H. R., & Gong, J. P. (2007). Large strain hysteresis and mullins effect of tough double-network hydrogels. Macromolecules, 40(8), 2919-2927.

[36] Lake GJ and Thomas AG. Proceedings of the Royal Society of London Series a-Mathematical and Physical Sciences 1967;300(1460):108-119.

[37] Y. Tanaka, K. Fukao and Y. Miyamoto, Eur. Phys. J. E, 2000, 3, 395

[38] Hugh R. Brown, A Model of the Fracture of Double Network Gels , Macromolecules, 2007, 40 (10), pp 3815–3818

[39] Y. Tanaka, Europhys. Lett., 2007, 78, 56005.

[40] Wang, X. and Hong, W., 2011. Pseudo-elasticity of a double network gel. Soft Matter, 7(18), pp.8576-8581.

[41] Zhao, X. (2012). A theory for large deformation and damage of interpenetrating polymer networks. Journal of the Mechanics and Physics of Solids, 60(2), 319-332.

[42] VHB tape，3M Product Number 4910，3M 2016, http://www.3m.com/

[43] Nylon Mandel Fabrics Tulle, http://www.walmart.com/ip/Nylon-Falk-Tulle-Fabric-White/19237863